Applied Water Science (2024) 14:129
https://doi.org/10.1007/s13201-024-02187-2

ORIGINAL ARTICLE

RSM versus ANN for modeling and optimization of magnetic adsorbent based on montmorillonite and $CoFe_2O_4$

Yiene Molla Desalegn[1] · Endrias Adane Bekele[2] · Getamesay Haile Dagnaw[3] · Sisay Asmare Marye[1] · Yared Daniel Reta[4]

Received: 12 January 2024 / Accepted: 22 April 2024

Abstract

A highly resourceful, environmentally benign, and recyclable magnetic montmorillonite composite (MMT/CF) was obtained through a simple one-step hydrothermal method and exhibited excellent Pb (II) removal. The as-synthesized adsorbent was then characterized by XRD, SEM–EDX, FTIR, BET, and TGA-DTA. The operating parameters including adsorbent dosage, initial Pb (II) concentration, solution pH, and time were studied. Also, a comparative approach was formed between response surface methodology (RSM) and artificial neural network (ANN) to optimize and model the removal efficiency of Pb (II) by MMT/CF. The results indicated that the ANN model was more precise and quite trusted optimization tool than RSM in consideration of its higher correlation coefficient ($R^2 = 0.998$) and lower prediction errors (RMSE = 0.851 and ADD = 0.505). Langmuir isotherm provided the best fit to the experimental data, and the maximum adsorption capacity was 101.01 mg/g. Additionally, the kinetic studies showed that the pseudo-second-order model fitted well with the experimental data. The magnetic MMT/CF composite possesses high adsorption capacity and is suitable for reuse. Therefore, this study shows that MMT/CF composite can be a potential adsorbent in Pb (II) uptake from aqueous media.

Keywords Montmorillonite/$CoFe_2O_4$ composite · Adsorption · Response surface methodology · Artificial neural network

Introduction

Nowadays, heavy metal ions cause various detrimental effects on both human health and the ecological system because they are non-biodegradable, toxic, and they tend to bio-accumulate in the food chain (Lu et al. 2023). These heavy metals, including lead, zinc, cadmium, copper, nickel, and chromium, are highly toxic even at low concentration. Among the heavy metals, lead (Pb) possesses a severe impact on human health. Pb (II) may lead to different forms of cancer, cardiovascular diseases, impaired renal functions, and neurological defects. Water decontamination, therefore, is an essential process in providing safe water for drinking and other practices. Different approaches have been developed for water treatment, such as flocculation, coagulation, biological methods, photocatalytic methods, and adsorption, to name just a few. The adsorption approach is the most popular and has several merits such as low cost, simplicity in design, high efficiency, and easy regeneration without yielding toxic products (Ren et al. 2023a, b).

Montmorillonite (MMT) is water-containing layered smectite clay, which has been increasingly used for the adsorption process due to its appealing features, such as large surface area, high porosity, ion exchangeability, and negatively charged surface (Maleki et al. 2023). Nevertheless, the separation of MMT from the liquid phase after adsorption is often complicated and time-consuming (Khodosova et al. 2022; Fan et al. 2023). Therefore, various modification systems are needed to deal with the separation problem. In this regard, spinel ferrites have been regarded as a promising adsorbent due to their physiochemical properties such as large surface area, strong magnetism, and high

✉ Yiene Molla Desalegn
yiene21ayl@gmail.com

1 Department of Mechanical Engineering, School of Mechanical and Chemical Engineering, Woldia Institute of Technology, Woldia University, Woldia, Ethiopia

2 Faculty of Materials Science and Engineering, Jimma Institute of Technology, Jimma University, Jimma, Ethiopia

3 Faculty of Computing and Informatics, Jimma Institute of Technology, Jimma University, Jimma, Ethiopia

4 Department of Materials Science and Engineering, Adama Science and Technology University, Adama, Ethiopia

Published online: 13 May 2024

adsorption performance (Fan et al. 2017). Because of these advantages, $CoFe_2O_4$ nanoparticles have been widely used to remove Pb (II) from aqueous solution. For example, (Ren et al. 2023a, b) synthesized $CoFe_2O_4$-graphene oxide nanocomposite for removal of Pb(II), and magnetic separation was applied, leading to lower cost and easier operation.

In recent years, it is more effective to use artificial intelligence to enhance modeling and optimization of process parameters (dosage, analyte concentration, solution pH, and contact time) than traditional methods. In most cases, the response surface methodology (RSM) comprises a central composite design (CCD), which has been commonly used to investigate the interactive effect of independent variables and then to boost the removal efficiency (Rasoulzadeh et al. 2020a, b). On the other hand, artificial neural networks (ANN) learn from experimental data and are capable of analyzing multivariate nonlinear and complex systems. As a result, it is more accurate and can replace the polynomial regression-based RSM modeling approach (Foroughi and Azqhandi 2020; Saber et al. 2021). Furthermore, many studies have been reported on the ANN-predicted model of Pb (II) removal from aqueous solution using functionalized bentonite (Lingamdinne et al. 2023a, b), thiosemicarbazone modified chitosan (Zaferani et al. 2019), polyamine-polyurea polymer modified with pyromellitic dianhydride(Kiraz et al. 2019), multiwall carbon nanotubes (Al-Jadir et al. 2023), and polyacrylamide cellulose supported Fe_3O_4 magnetic nanocomposites (Rasoulzadeh et al. 2020a, b). The results show that the ANN model was the most fitted model that accurately predicts Pb (II) removal efficiency.

To our knowledge, there have been no prior experimental report assessed synchronously by the comparison of RSM and ANN to optimize Pb (II) adsorption on MMT/CF composite. Hence, the main objective of this study is to evaluate the adsorption capacity of MMT/CF composite as eco-friendly and low-cost adsorbent in Pb (II) removal with the aid of the RSM and ANN application. Moreover, the adsorbent was synthesized by straight forward approach followed by characterization using XRD, SEM–EDX, FTIR, BET, and TGA-DTG.

Materials and methods

Reagents

Analytical grade chemicals such as cobalt (II) chloride hexahydrate ($CoCl_2.6H_2O$, 97%), ferric (III) chloride hexahydrate ($FeCl_3{\cdot}6H_2O$, 99%), hydrochloric acid (HCl, 37%), sodium hydroxide (NaOH, 99%), and lead nitrate ($Pb(NO_3)_2$, 99%) were obtained from Materials Science and Engineering Laboratories, Jimma Institute of Technology, Jimma, Ethiopia. Raw montmorillonite clay was collected from the Afar region, Ethiopia. Distilled water was used for all experiments.

Pre-treatment of montmorillonite

The raw Montmorillonite was dried at 100 °C for 4 h followed by crushing into powder. The sample was then washed with distilled water to remove water-soluble impurities. Afterward, the sample was dried for 20 h at 100 °C in the oven followed by grinding. It was then sieved through a 75-mesh to get a fine powder.

Synthesis of $CoFe_2O_4$ and montmorillonite/$CoFe_2O_4$ nanocomposite

$CoFe_2O_4$ was prepared according to the previous work with little modification (Jiang et al. 2021). The MMT/CF composite was also synthesized based on the synthesis of CF. Initially, 1.0 g of MMT was added in 50 mL of ethylene glycol and sonicated for 30 min to distribute the powders uniformly. Then, the necessary amount of $FeCl_3{\cdot}6H_2O$ and $CoCl_2{\cdot}6H_2O$ in a 2:1 ratio was added to the MMT suspension, followed by stirring for 60 min at room temperature. After that, 2-M NaOH solution was dropped to the solution under constant stirring to adjust the pH around 10.5, then stirring for 20 min. The resulting mixture was placed in a 100 mL Teflon-lined stainless-steel autoclaves, kept at 200 °C for 9 h, and cooled down to room temperature. Afterward, the product was washed three times with distilled water and ethanol and dried at 100 °C for 12 h, and then calcined at 400 °C for 3 h in a muffle furnace.

Characterization

X-ray powder diffraction (XRD-700, Shimadzu, South Korea) was used to examine the phase crystallinity of MMT/CF nanocomposite. To study the surface morphology and elemental composition, a scanning electron microscope coupled with energy-dispersive X-ray analysis (SEM–EDX) (COXIEM-30, Shimadzu, South Korea) was used. Fourier-transform infrared spectroscopy (FT/IR-4000 series, JASCO) was used to detect functional groups. Brunauer–Emmett–Teller (BET) using a Quantachrome analyzer (Nova station C, version 11.0) was employed to estimate the surface area and porosity of the MMT/CF based on the principle of adsorption/desorption of nitrogen at 77.3 K and 60/60 s (ads/des) equilibrium time. All the characterization tests were performed in the Materials Science and Engineering Laboratories, Jimma Institute of Technology, Jimma, Ethiopia.

Lead adsorption experiments

For the adsorption test, a stock Pb (II) solution of 1000 mg/L was prepared by dissolving $Pb(NO_3)_2$ into distilled water. Then, a sample of 25-mL-volume adsorbate solution of specified initial concentrations (15–55 ppm) was stirred at 250 rpm at room temperature using different adsorbent dosage in a 100-mL conical flask. Finally, atomic absorption spectrometer (ZEEnit 700P, Atomic Flame Mode, Analytik Jena) was used to analyze the residual Pb (II) in the filtrates. The pH of the solution was controlled by adding 0.1-M NaOH and 0.1-M HCl solutions. Magnetically separated adsorbents were used for the regeneration after drying in an oven at 100 °C for 2 h.

The adsorption capacity and removal efficiency of the adsorbent were then calculated using Eqs. (1 and 2) as follows:

$$q_e = \frac{V(C_o - C_e)}{m} \tag{1}$$

$$\eta(\%) = \frac{(C_o - C_t)}{C_o} \times 100 \tag{2}$$

where C_o and C_e (mg/L) are initial and residual concentration of Pb(II), C_t is the concentration at a given time, V (L) is the volume of the adsorbate, m (g) is mass of the adsorbent, q_e(mg/g) is the equilibrium adsorption capacity, and η (removal efficiency).

Experimental design and statistical analysis using RSM

The effect of independent parameters such as adsorbent dosage, initial concentration, solution pH, and contact time were optimized using CCD-RSM. The range of the process variables was wisely chosen for maximizing the removal efficiency. An increase in the adsorbent dosage led to increase in the amount of heavy metal ions adsorption on MMT/CF, and the adsorption removal decreased with increase in the initial Pb(II), which corresponded to ordinary rules of adsorption (Manzoor et al. 2024). Thus, the adsorption of Pb (II) onto MMT/CF was studied by varying the adsorbent dosage (0.15–0.55 g/L), with a dose of 0.55 g/L being possible to allow for all Pb (II) to be removed by the adsorbent. The pH range was chosen to be (3.5–7.5) because at low pH values, there is competition between Pb (II) and H^+, while at high pH values the Pb(II) ions could be converted to Pb(OH) (Kochar et al. 2023). A short range of contact time (20–60 min.) could also allow a more suitable basis for experiments, ensuring that the impact of duration could be well addressed.

Table 1 shows the levels of the four independent variables for Pb(II) removal.

ANN modelling

Nowadays, artificial neural network (ANN) is considered as a well-known deep learning model that simulates the functions of human neurons through a network of interconnected neurons.

Figure 1 shows the proposed ANN architecture which consists of four input nodes in the input layer, a hidden layer with nine neurons, and a single output node. The input variables applied in this investigation include dose (g/L), concentration (mg/L), pH, and duration (min), whereas the corresponding outputs are represented by the response variable R (%). The model uses KerasTuner for hyperparameter optimization, to determine the optimal configuration of the model.

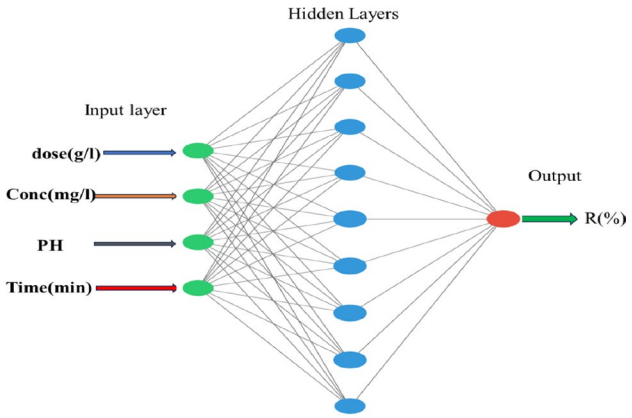

Fig. 1 General layout of ANN Model

Table 1 Level of independent variables

Variables	Variable coding	Units	$-\alpha$	-1	0	$+1$	$+\alpha$
Adsorbent dosage	*A*	g/L	0.15	0.25	0.35	0.45	0.55
Initial Pb (II) conc	*B*	mg/l	15	25	35	45	55
Solution pH	*C*		3.5	4.5	5.5	6.5	7.5
Time	*D*	Min	20	30	40	50	60

Results and discussion

XRD analysis

The powder XRD patterns of MMT, $CoFe_2O_4$, and MMT/$CoFe_2O_4$ nanocomposite samples are presented in Fig. 2a–c, respectively. For MMT/ $CoFe_2O_4$ nanocomposite, characteristics peaks at a 2θ of 7°, 20.4°, 36.1°, 54.5°, and 62.1°, correspond to the crystallographic planes of (001), (100), (105), (210), and (300), could be ascribed to MMT (the JCPDS pattern 09–0432) (Moja et al. 2020). These peaks are the same as those observed in Fig. 2a, with minor impurities of quartz, kaolinite, and dolomite. However, the diffraction peaks at a 2θ of 18.3°,30.15, 35.5°, 37.1°, 43.2°, 53.6°, 57.1°, and 62.65° belong to the crystal indexes of (111), (220), (311), (222), (400), (422), (511), and (440), respectively. These results are consistent with standard XRD data of spinel $CoFe_2O_4$ (JCPDS: 01-077-0426), indicating the presence of $CoFe_2O_4$ in the composite (Wang et al. 2018). Such results are also similar to those displayed in Fig. 2b. Moreover, the composite exhibited a lower d_{001} values, which confirms the successful loading of the MMT surface (Thamer, Aldalbahi et al. 2019). The approximate crystallite size of the composite was also calculated to be 22.6 nm according to the Debay–Scherer equation (Basak et al. 2022), $D = K/\beta\cos\theta$, where the constant k is 0.89, λ is the X-ray wavelength, β is the full-width half maximum, and θ is the Bragg's angle.

SEM–EDX analysis

The morphological properties MMT and MMT/CF composite are presented in Fig. 3a, b, respectively. The as-synthesized MMT (Fig. 3a) depicted a microstructure with smooth surface in which the MMT particles are distributed with less aggregations (Chu et al. 2020). However, the surface morphology of MMT/CF nanocomposite revealed a rough morphology with high agglomeration and uneven particle distribution (Fig. 3b). This is due to the magnetic property of CF (Yuan et al. 2009). Hence, the as-prepared MMT/CF composite could provide an efficient adsorption process to the targeted Pb (II) due to the available surface-active sites and its porous nature.

Energy-dispersive X-ray (EDX) analysis was done to further examine the elemental composition of the samples (Fig. 4a and b). In Fig. 4a, the EDX spectrum of MMT shows the existence of Na, Mg, Al, Si, and O without any more peaks. Also, The EDX spectrum of MMT/CF composite indicated the presence of Na, Mg, Al, Si, O, Co, and Fe in the structure (Fig. 4b).

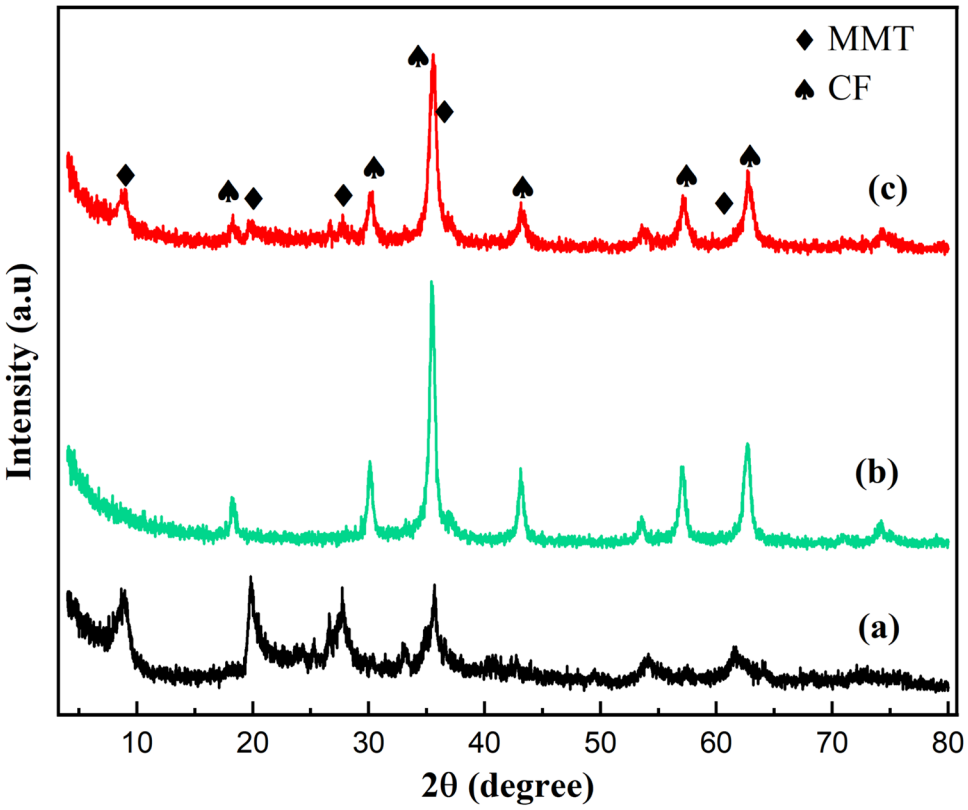

Fig. 2 XRD pattern of MMT (**a**), CF (**b**), and MMT/CF composite (**c**)

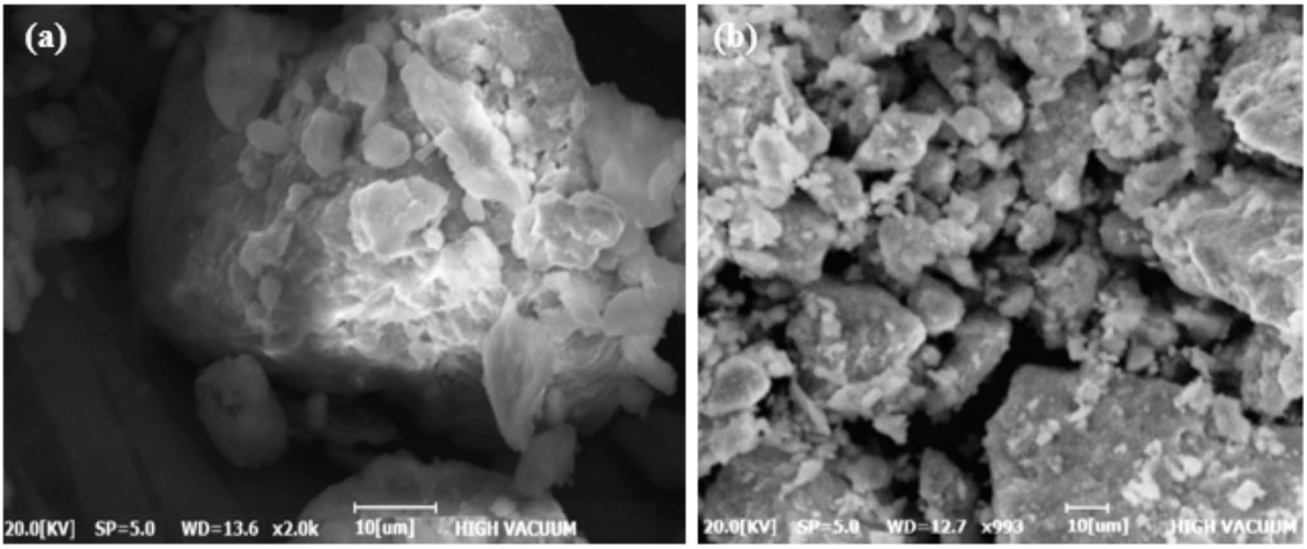

Fig.3 SEM micrograph of **a** MMT and **b** MMT/CF

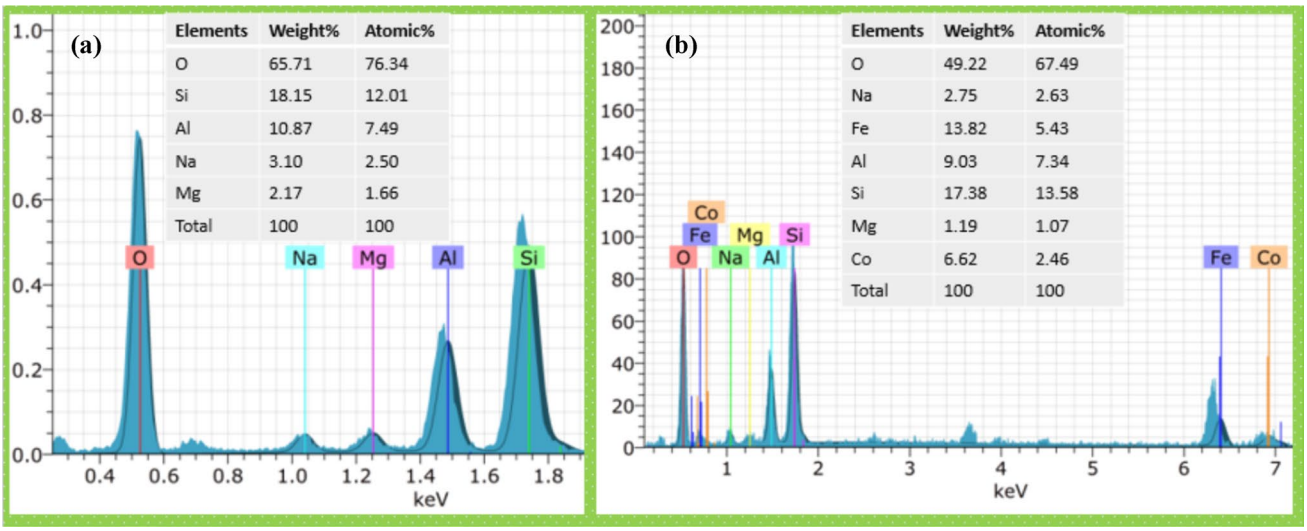

Fig. 4 EDX analysis of **a** MMT and **b** MMT/CF

FTIR analysis

In order to identify the presence of functional groups on the surface of prepared adsorbent, it was determined by FTIR analysis (Fig. 5a and b). In the structure of MMT and MMT/CF composite, the peaks at 3445 and 1636 cm^{-1} are attributed to the existence of O–H and H–OH stretch vibrations in these materials (Chang et al. 2023). The intensity of the peaks was reduced for MMT/CF composite as compared to MMT, suggesting that the composite has less bonded H_2O molecules. The FT-IR spectrum of pristine MMT exhibited characteristic absorption peaks at 1037 cm^{-1} (Si–O or Al–O) (Tayyebi et al. 2015). The absorption peak of 614 cm^{-1} displayed that MMT/CF corresponds to the valence vibrational bond of metal–oxygen bond (Co–O and Fe–O) (Idehara et al. 2023). It should be noted that the area of the peak and the intensity of the peaks found in the as-synthesized composite changed significantly, which may be attributed to the interaction of CF with MMT layer (Foroutan et al. 2020).

BET analysis

The BET surface area, pore volume, and pore size of the prepared MMT/CF are listed in Table 2. The calculated

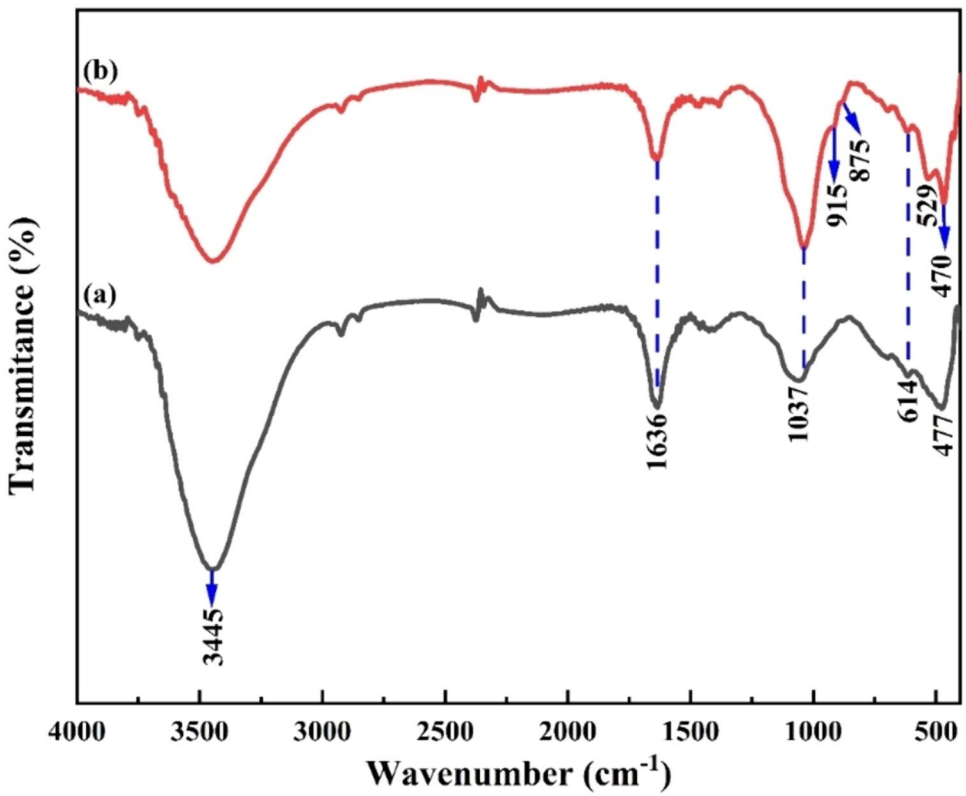

Fig. 5 FTIR spectra of **a** MMT and **b** MMT/CF composite

Table 2 BET analysis of MMT/CF composite

Adsorbent	BET surface area (m^2/g)	Pore volume (cm^3/g)	Pore diameter (nm)
MMT/CF	243.56	0.298	8.91

surface area, pore volume, and pore diameter were found to be 243.56 m^2/g, 0.298 cm^3/g, and 8.91 nm, respectively. This high surface area with high porosity is the main factor behind adsorbing Pb (II) ions on the surface of MMT/CF.

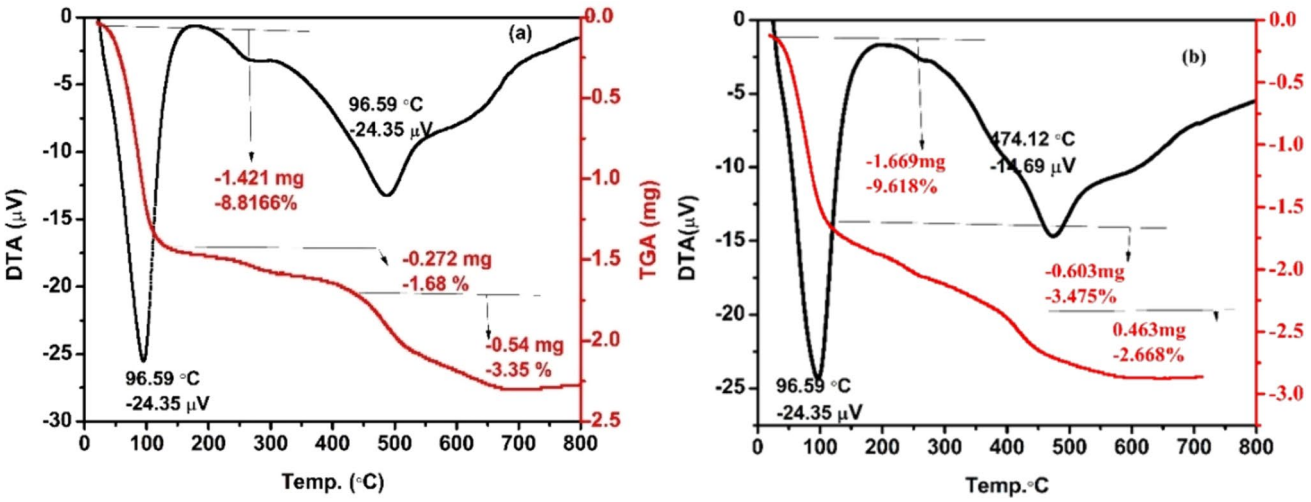

Fig. 6 TGA-DTA analysis of **a** MMT and **b** MMT/CF composite

Thermal property analysis

The thermal analysis for MMT clay and magnetic composites of MMT/CF are shown from TGA and DTA curves. As shown in Fig. 6a, b, the weight of MMT and MMT/CF was significantly reduced in three stages. The first stage of weight loss for MMT and MMT/CF composite was 8.816%, 9.618%, respectively. The primary cause for this weight loss is the evaporation of the water molecule from their structure (Alekseeva et al. 2019). The second weight loss was determined to be 1.668% and 3.475% for MMT and MMT/CF, respectively. This is due to dihydroxylation, clay decomposition, and decarburization of cobalt ferrite particles. The third weight loss reaches up to 800 °C due to the release of OH-groups from the structure. Overall, the sum of weight loss of the MMT (13.846%) < MMT/CF (15.761%). The results suggest that the MMT is more stable than the magnetic composite (Larraza et al. 2012).

Modeling of Pb (II) removal by RSM-CCD

With the aid of the RSM-CCD method, the combined effect of four independent factors on the process response was investigated to set the optimal values of the process parameters. In this work, a total of 30 experimental runs were carried out, 24 = 16 cube points, six replications at the center point and eight axial points The experimental removal efficiency of Pb (II) relative to the software (Design-Expert 13) prediction and their residuals are presented in Table 3.

As shown in Table 4, the quadratic model is the most fitting model as supported by the largest values of R^2 (0.9953), adjusted R^2 (0.9909), and predicted R^2 (0.9853) with a small

Table 3 The relationship between the actual values and results predicted by RSM and ANN

						Pb (II), removal, %			
						RSM		ANN	
Run	A	B	C	D	Experimental	Predicted	Residual	Predicted	Residual
1	0	0	0	0	88.66	89.67	−1.01	89.27	−0.61
2	−1	−1	1	1	71.67	71.02	0.6462	71.72	−0.05
3	0	0	0	−2	47.76	46.94	0.8208	47.82	−0.06
4	0	0	0	0	89.32	89.67	−0.3467	89.27	0.05
5	1	1	−1	−1	40.56	42.94	−2.38	38.76	1.8
6	0	2	0	0	49.06	48.63	0.4258	49.13	−0.07
7	1	−1	1	1	95.48	95.41	0.07	95.40	0.08
8	0	0	0	2	70.36	71.00	−0.6392	70.35	0.01
9	−1	−1	1	−1	60.75	59.94	0.8062	60.70	0.05
10	−1	1	1	−1	37.99	39.37	−1.38	38.25	−0.26
11	1	1	1	1	71.44	71.60	−0.1554	71.66	−0.22
12	1	−1	1	−1	83.53	84.03	−0.4954	83.55	−0.02
13	0	0	0	0	94.88	89.67	5.21	89.27	5.61
14	0	0	2	0	62.46	63.24	−0.7825	62.57	−0.11
15	−1	−1	−1	−1	45.47	47.05	−1.58	45.55	−0.08
16	−1	1	−1	−1	33.79	32.31	1.48	33.77	0.02
17	0	0	−2	0	35.64	34.68	0.9642	37.16	−1.52
18	0	0	0	0	88.34	89.67	−1.33	89.27	−0.93
19	−1	1	1	1	54.67	53.81	0.8613	54.77	−0.1
20	0	−2	0	0	88.95	89.19	−0.2442	88.94	0.01
21	0	0	0	0	88.21	89.67	−1.46	89.27	−1.06
22	1	1	1	−1	55.89	54.86	1.03	55.57	0.32
23	−1	−1	−1	1	54.89	54.37	0.5196	54.89	0
24	−2	0	0	0	41.95	42.10	−0.1475	41.74	0.21
25	1	1	−1	1	56.67	55.92	0.7479	55.04	1.63
26	1	−1	−1	−1	66.98	66.29	0.6929	66.7	0.28
27	−1	1	−1	1	41.74	42.98	−1.24	42.21	−0.47
28	0	0	0	0	88.59	89.67	−1.08	89.27	−0.68
29	2	0	0	0	79.45	79.12	0.3292	79.94	−0.49
30	1	−1	−1	1	75.56	75.91	−0.3521	75.54	0.02

Table 4 lack of fit test

Source	Sum of squares	Df	Mean square	*F* value	*p* value
The sequential model sum of squares					
Linear vs Mean	6616.17	4	1654.04	8.23	0.0002
2FI vs Linear	162.07	6	27.01	0.1055	0.9948
Quadratic vs 2FI	4810.27	4	1202.57	329.37	< 0.0001
Residual	44.28	7	6.33		
Source	Std. Dev	R^2	Adjusted R^2	Predicted R^2	PRESS
Model summary statistics					
Linear	14.18	0.5682	0.4992	0.4759	6102.25
2FI	16.00	0.5822	0.3622	0.2878	8292.72
Quadratic	1.91	0.9953	0.9909	0.9853	171.36

standard deviation (1.91). Maximized value of the predicted R^2 and the adjusted R^2 implies that the model is significant [36]. Furthermore, the *P* value of the quadratic model is lower than 0.0001, indicating the significance of the model.

Accordingly, the quadratic model correlates the four independent variables to the response (R) can be described by the following Eq. (3).

$$R = +89.67 + 9.26A - 10.14B + 7.14C + 6.02D - 2.15AB + 1.21AC - 1.46BC - 7.26A^2 - 5.19B^2 - 10.18C^2 - 7.67D^2 \quad (3)$$

where R (%) is the removal efficiency of Pb (II), A is the dosage of MMT/CF, B is the initial concentration, C is the pH, and D is the contact time.

Analysis of residuals was also done to validate the significance of the selected model. The difference between the experimental value and the predicted one is called Residual (Simsek et al. 2022). Lower values of the residuals imply the significance of the suggested model by CCD.

The variation of normal probability against externally studentized residuals is shown in Fig. 7a. This profile shows that all the externally studentized residual points are distributed along the line indicating the significance of the selected model. This was further supported by the plot of a random

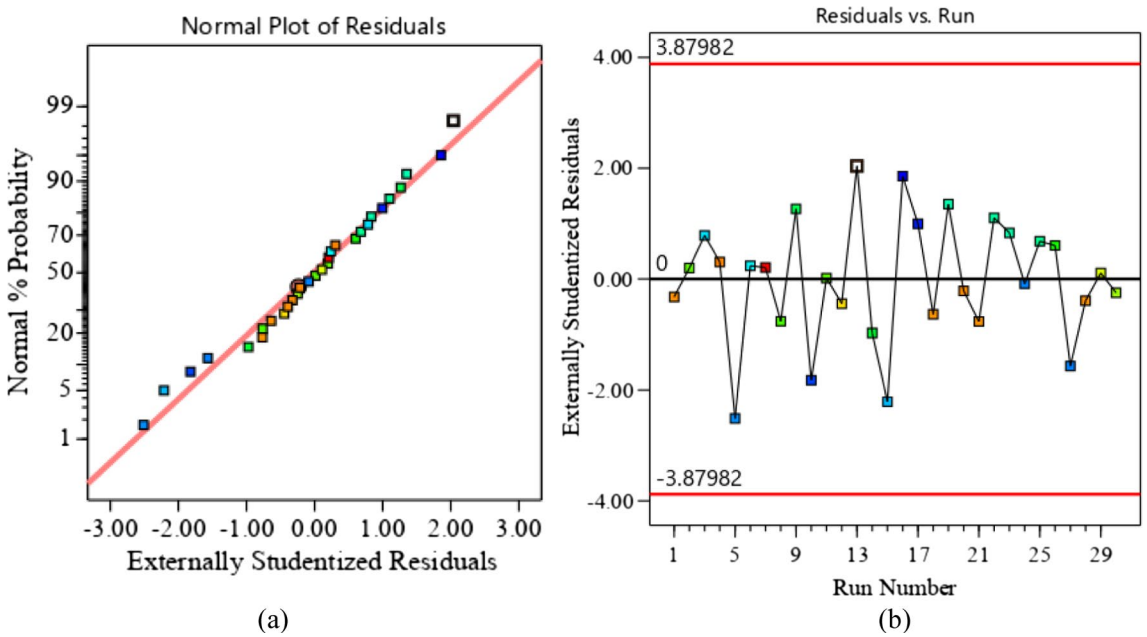

Fig. 7 Normal probability plot of externally standardized residuals (**a**) and the plot of residuals versus run number for removal of Pb (II) (**b**)

scatter of residuals versus the expected values (Abu-Hamdeh et al. 2021) (Fig. 7b). The plot revealed that the points follow a straight line, confirming the model is significant.

ANOVA examination

Analysis of variance (ANOVA) table was generated to confirm the accuracy of the equation Table 5. This evaluation is performed by the model *F* statistic (*F* value) and the probability value (*P* value). A model is said to be significant, if *F* value obtained is high (Sultana et al. 2020). Herein, the model *F* value of 226.72 together with the low lack-of-fit *F* value (0.3210) implies the significance of the model. Furthermore, *P* values less than 0.0500 indicate model terms are significant.

The coefficient of determination R^2 was calculated to be 0.9953, indicating that 99.53% of the variability in the response can be explained by the quadratic model, and therefore, only 0.47% of the observed variability is not explained by the model. The high value of adjusted R^2 (0.9909) further confirms that the model is favorable. The predicted R^2 of 0.9853 is in reasonable agreement with the adjusted R^2 representing the effectiveness of the model.

Table 5 ANOVA result for Pb (II) removal from CCD

Source	Sum of Squares	df	Mean square	*F* value	*p* value
Model	11,588.51	14	827.75	226.72	< 0.0001
A-dose	2056.09	1	2056.09	563.15	< 0.0001
B-conc	2467.67	1	2467.67	675.88	< 0.0001
C-pH	1224.08	1	1224.08	335.27	< 0.0001
D-time	868.33	1	868.33	237.83	< 0.0001
AB	73.96	1	73.96	20.26	0.0004
AC	23.47	1	23.47	6.43	0.0228
BC	33.93	1	33.93	9.29	0.0081
A^2	1447.44	1	1447.44	396.44	< 0.0001
B^2	738.29	1	738.29	202.21	< 0.0001
C^2	2840.74	1	2840.74	778.06	< 0.0001
D^2	1615.43	1	1615.43	442.46	< 0.0001
Residual	54.77	15	3.65		
Lack of fit	21.41	10	2.14	0.3210	0.9405
Pure error	33.35	5	6.67		
Cor total	11,643.27	29			
R^2	0.9953				
Adjusted R^2	0.9909				
Predicted R^2	0.9853				
Adeq Precision	48.1859				
Std. Dev	1.91				
C.V. %	2.92				
PRESS	171.36				

The signal-to-noise ratio (48.186) was evaluated with adequate precision, implying that the model can be used to navigate the space of design. The low value of the coefficient of variance ($C{\cdot}V = 2.92\%$) indicates that the deviation between the actual and prediction values is low.

The reasonably low value of sum of squares of prediction error (PRESS = 171.36) suggests the chance of error during the experiment, and thus the predicted values are low.

Three-dimensional responses and contour plots

The 3D response surfaces plots help to investigate the effect of the independent variables and their interactions on the dependent one (Fig. 8a–c).

The adsorbent dosage value is one of the most important variables in the removal of heavy metal ion (Weyrich et al. 2023). As can be seen from Fig. 8a, b, increasing the adsorbent dose increases the removal efficiency of the adsorbent, because it increases the number of active sites, which could adsorb more Pb (II) ions; thus, increases the removal efficiency (Cheblaoui et al. 2023). As shown in Fig. 8a, the increase in the adsorbent dosage from 0.25 to 0.45 g increases the removal efficiency from 76.1% to 98.8%. Figure 8a, c shows that increasing the initial concentration decreases the removal of Pb (II) ions, because at higher initial concentrations, the Pb (II) ions forms an aggregation and overlap on the surface of the composite, reducing the surface area on the adsorbent and as a result, the adsorption efficiency decreases, which is consistent with the results of a previous study. The maximum removal of Pb (II) ions at a concentration of 25 mg/L was 76.34%. However, the lowest removal of Pb (II) ions at a concentration of 45 mg/L was 58.70%.

The pH has also significant effect on removal efficiency as shown in Fig. 8c. It can be seen that the maximum removal efficiency of Pb (II) was attained at pH 6.0. This is because at low pH values, there is competition between Pb (II) and H^+ to occupy the active sites on the adsorbent surface, as a result the removal efficiency decreases. Nevertheless, at high pH values, the adsorbent surface becomes negatively charged, therefore, Pb(II) ions are converted to $Pb(OH)_2$ (Huang et al. 2017).

In general, the optimum values of the independent variables for the maximum Pb(II) removal efficiency were found to be 0.45 g adsorbent dosage, 26.94 mg/L initial Pb (II) concentration, 6.01 solution pH, and 49.2 min. time. Considering these optimum conditions, the predicted and experimental removal efficiencies of Pb(II) were 99.08 and 97.88%, respectively.

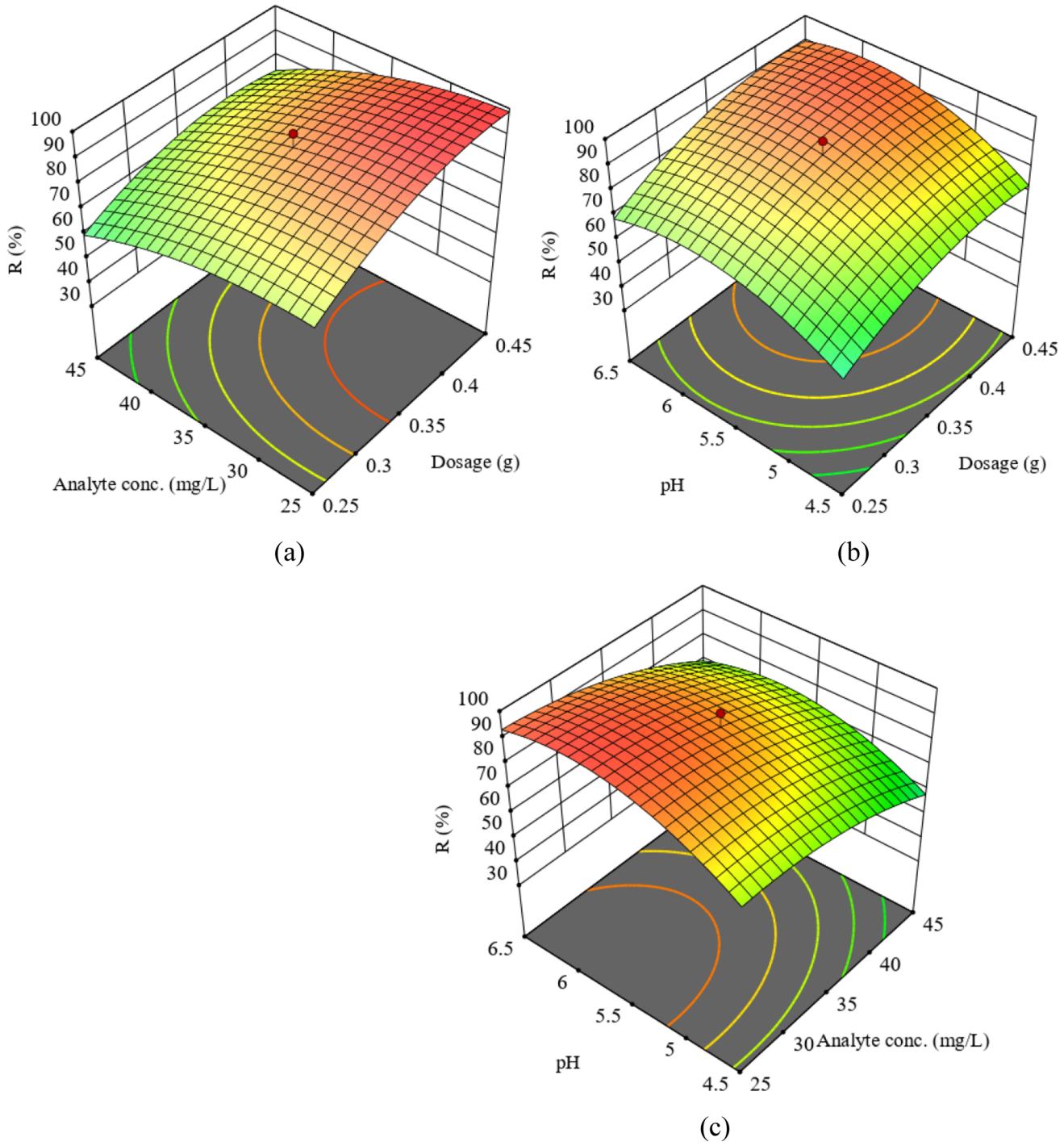

Fig. 8 Three-dimensional and contour plots showing the effects of **a** analyte concentration and adsorbent dosage, **b** pH and adsorbent dosage, and **c** pH and adsorbent dosage on the removal efficiency of MMT/CF toward Pb (II)

Modeling of Pb (II) removal by ANN

The ANN architecture with the sigmoidal function now becomes the most widely used technique for modeling the removal process of Pb (II) by several adsorbents (Lingamdinne et al. 2023a, b). The ANN was trained by the RSM matrix and their respective experimental response. The network has four input variables (adsorbent dosage, initial Pb (II) concentration, solution pH, and time) and one output variable (Pb (II) removal). Training and validation can reduce the errors associated with the ANN model (Vázquez-Sánchez et al. 2023). The network was trained until the R^2

attained its maximum value and RMSE, MAD and ADE reached the lowest values. Additionally, each experimental run along with the predicted values based on the ANN model, was assessed and tabulated as compared with the experimental and predicted RSM values in Table 8. Furthermore, the residuals are found to be very low at all runs, implying that the ANN can best describe the experimental value.

Figure 9 illustrates the experimental and ANN-predicted values. The model's ability to predict the response variable is confirmed by high R^2 value and decreased RMSE value.

RSM versus ANN models

In this work, a comparative study was investigated between RSM and ANN models using on several statistical parameters, including the coefficient of determination (R^2), root mean square error (RMSE) and absolute average deviation (AAD) (Oskui et al. 2019; Onu et al. 2021, Prabhu et al. 2023).

The R^2 was calculated using Eq. (4):

$$R^2 = \frac{\sum_{i=1}^{N}\left(Y_{i,\exp} - \overline{Y}_{\exp}\right)\left(Y_{i,\text{pred}} - \overline{Y}_{\text{pred}}\right)}{\left(\sqrt{\sum_{i=1}^{N}\left(Y_{i,\exp} - \overline{Y}_{\exp}\right)}\right)\left(\sqrt{\sum_{i=1}^{N}\left(Y_{i,\text{pred}} - \overline{Y}_{\text{pred}}\right)}\right)} \quad (4)$$

where N is the number of experimental data, $Y_{i,\exp}$ is the ith data point of experimental output, $\overline{Y}_{\exp}$ is mean value of experimental output, $Y_{i,\text{pred}}$ is the ith data point of predicted output, and $\overline{Y}_{\text{pred}}$ is the mean value of predicted output.

The RMSE and AAD was calculated using Eqs. (5) and (6), respectively.

$$\text{RMSE} = \sqrt{\frac{\sum_{i=1}^{n}\left(Y_{\text{pre}} - Y_{\exp}\right)^2}{n}} \quad (5)$$

The AAD was calculated using Eq. (6)

$$\text{AAD} = \left[\frac{\sum_{i=1}^{n}\left(\left|Y_{\text{pre}} - Y_{\exp}\right| / Y_{\exp}\right)}{n}\right] \times 100 \quad (6)$$

Y_{pre} is the predicted response, $Y_{\exp}$ is the experimental response, and n is the number of experiments ($n = 30$).

The statistical parameters that measure and compare the accuracy of both models were estimated based on (Table 6). Generally, the high value of R^2 and lower values of the RMSE and AAD determines the modeling ability of a given model (Saber et al. 2021). RMSE is 1.3587 and 0.851 for RSM and ANN, respectively, which illustrates that the predicted value using ANN has less deviation compared to RSM. The obtained R^2 values for CCD and ANN are 0.9953 and 0.998, respectively. Furthermore, the AAD value

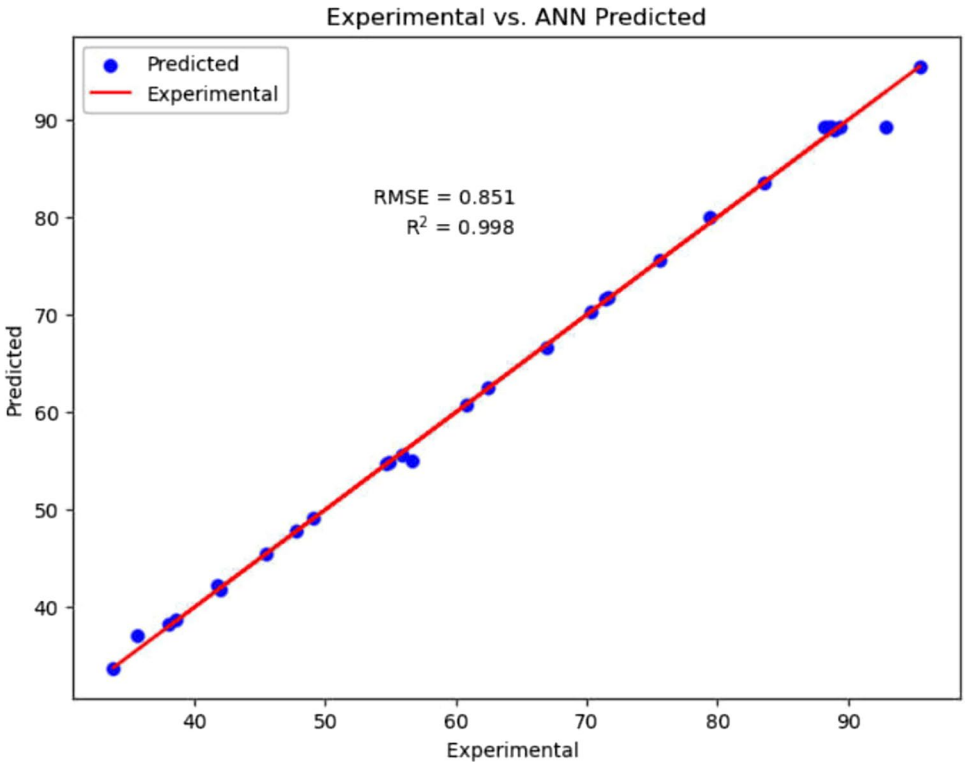

Fig. 9 The experimental and predicted values by ANN

Table 6 Comparison of the predictive abilities of RSM and ANN models

Measure	CCD	ANN
Coefficient of determination (R^2)	0.9953	0.998
Root of mean square error (RMSE)	1.3587	0.851
Absolute average deviation (AAD)	1.683	0.505

of CCD-RSM (1.683) was lower than ANN (0.505). Hence, ANN has more prediction ability in comparison to RSM. Because ANN can best describe any kind of nonlinearity with no need for a standard experimental design (Huang et al. 2017). Conversely, RSM is preferable to ANN because it gives information about the effect of each parameters and their interactive effects (Ahmadi et al. 2021). Thus, ANN model is more suitable and quite trusted.

Adsorption isotherm analysis

The equilibrium adsorption process was studied based on Freundlich and Langmuir isotherm models. The Langmuir isotherm shows monolayer formation of Pb (II) due to homogenous adsorption process on the surface of the adsorbent. Langmuir isotherm equation is given as Eq. (7) (Romero-González et al. 2006):

$$\frac{C_e}{q_e} = \frac{1}{q_{\max} K_L} + \frac{C_e}{q_{\max}} \tag{7}$$

where K_L is the Langmuir isotherm coefficient and $q_{\max}$ is the maximum monolayer adsorption capacity.

Additionally, the separation factor (R_L) may be used to determines the favorability of Langmuir adsorption model, expressed as follows (Eq. 8) (Zhao et al. 2021).

$$R_L = \frac{1}{1 + K_L C_o} \tag{8}$$

According to R_L values, the isotherm is favorable ($0 < R_L < 1$), unfavorable ($R_L > 1$), irreversible ($R_L = 0$), and linear adsorption ($R_L = 1$) (Moustafa 2023).

On the other hand, Freundlich adsorption isotherm is for non-uniform distribution of adsorbate on heterogeneous surface. Freundlich adsorption isotherm equation is given as Eq. (9)

$$\ln q_e = \ln K_F + \frac{1}{n} \ln C_e \tag{9}$$

where K_F is the Freundlich adsorption coefficient, and n is the Freundlich exponent (Velarde et al. 2023).

Table 7 and Fig. 10 give the parameters for the two isotherm models. The calculated values indicated that Langmuir isotherm is the best fit to the adsorption equilibrium data of Pb(II) removal. Furthermore, R_L value was between 0 and 1, confirming that the Langmuir adsorption was significant. Therefore, the maximum monolayer adsorption capacity ($q_{\max}$) was found to be 101.01 mg/g.

Table 7 Isotherm models and their parameters

Isotherm models	Parameters	Values	R^2
Freundlich	N	1.731	0.9648
	K_F	19.47	
Langmuir	$q_{\max}$ (mg/L)	101.01	0.9907
	K_L (1/mg)	0.5657	
	R_L	0.0378	

Kinetic modeling

The pseudo-first-order and pseudo-second-order models were applied to study the rate of Pb (II) adsorption based on the obtained data (Fig. 11). The linear equation for the pseudo-first order and pseudo-second order for MMT/CF composite are calculated using Eqs. (10) and (11), respectively.

$$\log\left(q_e - q_t\right) = \log q_e - \frac{K_1}{2.303} t \tag{10}$$

$$\frac{t}{q_t} = \frac{1}{K_2 q_e^2} + \frac{1}{q_e} t \tag{11}$$

where q_t and q_e(mg/g) are the amount of Pb (II) adsorbed (g) at time t (min) and at equilibrium, respectively. K_1(min^{-1}) and K_2 (g mg^{-1} min^{-1}) are the rate constants of pseudo-first-order and pseudo-second-order models, respectively. According to the calculated parameters in Table 8, the experimental data were favorably predicted by the pseudo-second-order kinetic model because of the high R^2 values. Moreover, the calculated q_e for the pseudo-second order agreed reasonably well to the actual q_e values.

Comparison of MMT/CF with other adsorbents

The adsorption capacity of MMT/CF for Pb(II) removal was compared with other adsorbent materials and is presented in Table 9. It can be seen that MMT/CF composite was higher than previously reported works in terms of adsorption capacity (101.01 mg/g).

Proposed mechanism for the adsorption process

Surface complexation, ion exchange, and electrostatic interactions are key in the adsorption of heavy metal ions (Alcalde-Garcia et al. 2023). Surface complexation, which

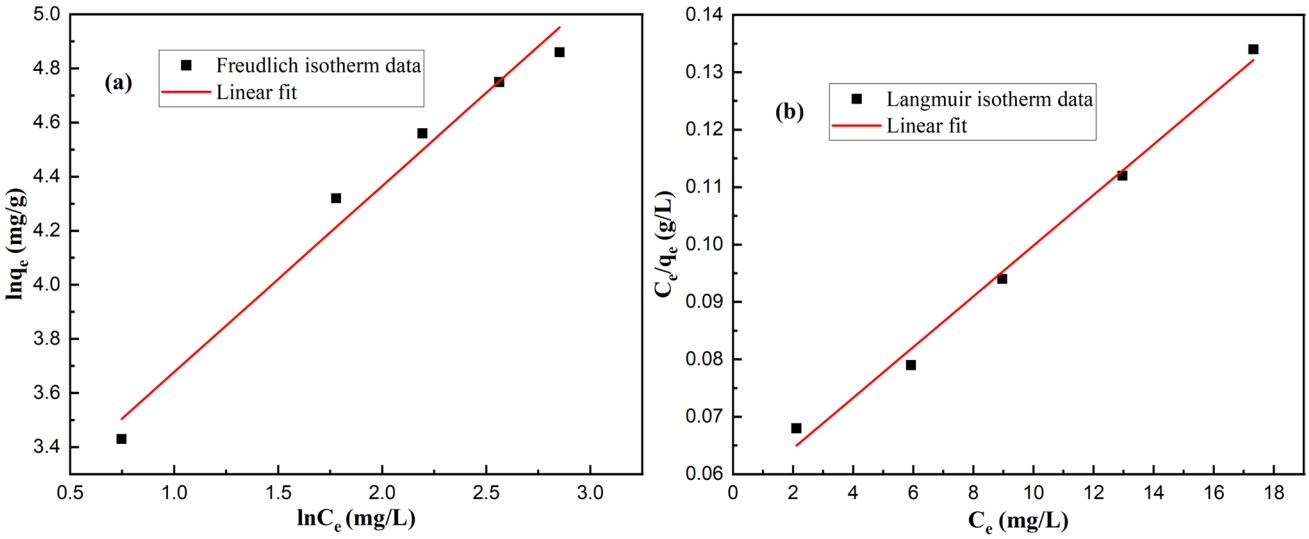

Fig. 10 Freundlich (**a**) and Langmuir (**b**) isotherm models

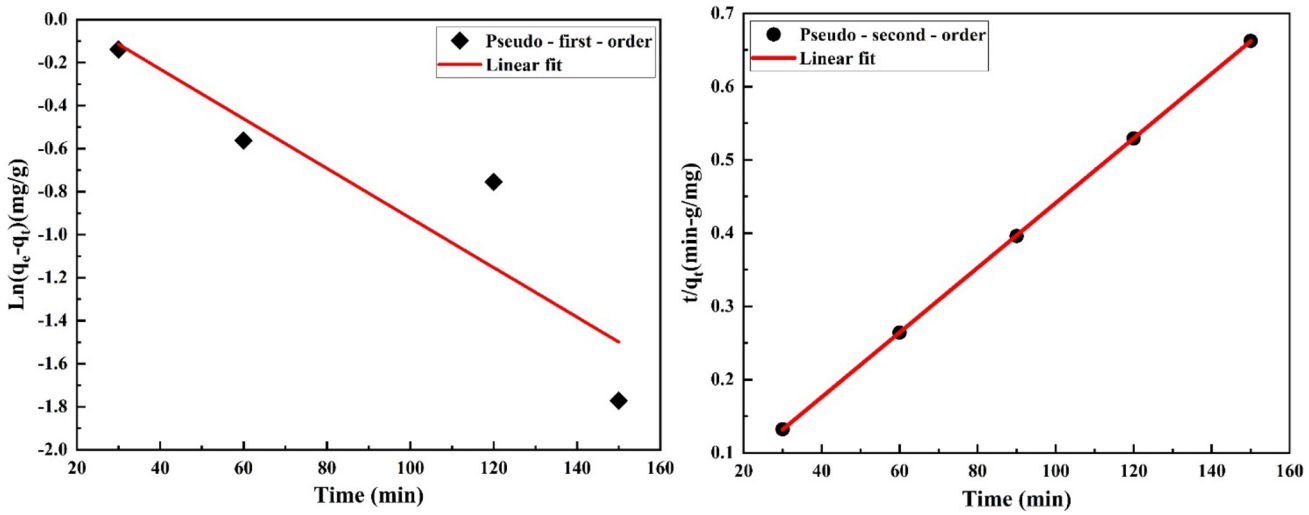

Fig. 11 Pseudo-first-order and pseudo-second-order kinetics for adsorption of Pb (II)

Table 8 Adsorption kinetic parameters of Pb(II) onto MMT/CFcomposite

Adsorbent	$q_{e,exp}$ (mg/g)	Pseudo-first-order			Pseudo-second-order		
		$q_{e,cal}$ (mg/g)	K_1(min^{-1})	R^2	$q_{e,cal}$ (mg/g)	K_2(min^{-1})	R^2
MMT/CF	101.01	8.255	0.0375	0.7033	99.01	0.00761	0.9926

is the ability of heavy metals to form multiatomic structures when they interact with functional groups in the adsorbent material. As can be seen from FTIR graph (Fig. 5), there are abundant hydroxyl group on MMT/CF composite, indicating that Pb(II) can interacts with –OH to form hydroxy complexes (-O-Pb) (Jiang et al. 2018). The "ion-exchange" process refers to the exchange of cationic pollutants with the interlayer cations on the adsorbent and adsorption of Pb(II) could be ion-exchange controlled process. Moreover, the other means of interaction between the Pb(II) and the adsorbent is electrostatic interaction because Pb(II) has a strong affinity toward the negatively charged MMT and hydroxyl (OH^-) ions. Overall, the adsorption of Pb(II) onto MMT/CF composite may be driven by a combination of several steps: transportation of the Pb(II) to the adsorbent surface from aqueous solution followed by adsorption onto

Table 9 Comparison of MMT/CF composite with other adsorbents for Pb(II) removal

Adsorbents	pH	Isotherms	q_m (mg/g)	References
Montmorillonite	6	Freundlich	31.1	Gupta and Bhattacharyya (2008)
MMT-K10	5	Langmuir	40.86	Hamidi et al. (2023)
Lcys grafted MMTNS	6	Langmuir	46.92	Fan et al. (2023)
Magnetic bentonite	5	Langmuir	80.44	Zou et al. (2019)
Bentonite-Chitosan composites	6	Langmuir	94.6	Majiya et al. (2023)
Kaolinite	6.5	Langmuir	61.5	Tian et al. (2022)
Extracellular polymeric substances (EPS)	6	Langmuir	99.5	Wei et al. (2016)
Amino-Functionalized Magnetite/Kaolin Clay	4.5	Langmuir	86.1	Qin et al. (2016)
MMT/CF	6	Langmuir	101.01	This work

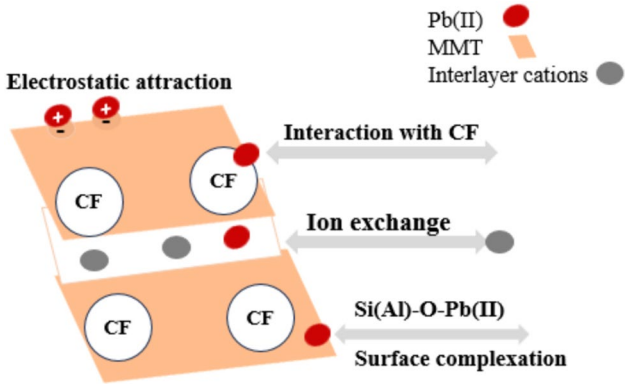

Fig. 12 Schematic diagram showing the possible adsorption mechanisms of Pb(II) by MMT/CF composite

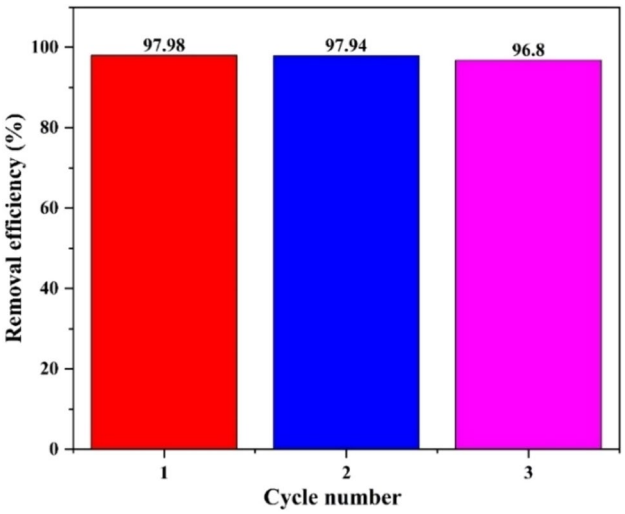

Fig. 13 Removal efficiency at diferent adsorption–desorption cycles

the adsorbent surface, and transport within the adsorbent particle (Raji et al. 2023). However, it is noteworthy that different literatures might verify adsorption mechanisms in a different way. Figure 12 illustrates possible mechanisms of Pb(II) onto the MMT/CF composite.

Reusability of the adsorbent

The reusability process was cost-effective and reasonable for the Pb(II)-loaded adsorbent. The adsorbent was regenerated under optimum conditions. Also, the reusability of MMT/CF composite to remove Pb(II) from aqueous solution was tested up to three cycles of adsorption–desorption. As can be seen form Fig. 13, as the adsorption–desorption steps increased, the removal efficiency of the adsorbent toward the adsorbate decreased (Elgarhy et al. 2022). The decrease in removal efficiency may be attributed to the incomplete desorption of Pb(II) from the surface of the adsorbent or due to the loss of active sites in the adsorbent (Jiang et al. 2018). The removal efficiency of the Pb(II) using the present adsorbent was 97.98, 97.94, and 96.8% in the first, second, and third cycles, respectively. Similar results have been reported for the regeneration of MMT-based adsorbent (Irawan et al. 2019; Wang et al. 2021). Overall, MMT/CF composite can be used repeatedly for three cycles with little reduction in the removal efficiency toward Pb(II) ions in aqueous solutions.

Conclusion

In this study, a composite of MMT and CF was effectively used to remove Pb(II) from aqueous solution. The adsorbent was characterized using XRD, SEM–EDX, FTIR, BET, and TGA-DTA. The CCD-based RSM was utilized to optimize several input variables, including adsorbent dosage, initial Pb (II) concentration, solution pH, and time. The RSM model predicted an optimal Pb (II) removal efficiency of 99.08% at 0.45 g/L and 26.94 mg/L and 6.02 and 49.2 min and validated experimentally as 97.88%. Determination coefficient (R^2), Mean-Square Error (MSE), and Absolute average deviation (AAD) were used to evaluate the operational conditions for the removal of Pb(II) using the MMT/CF. Even though both models could reasonably examine

the correlation of response variable with independent factors, the ANN is more precise than the RSM to describe the process data. The R^2, MSE, and ADD values of ANN were found to be 0.998, 0.851, and 0.5049, respectively. As can be seen from the isotherm and kinetics study, the adsorption process followed Langmuir isotherm and pseudo-second-order kinetics. Also, the synthesized adsorbent was stable for three-round tests toward the Pb(II) removal. Therefore, according to the obtained results, the MMT/CF can be considered as a cost-effective and sustainable adsorbent for adsorptive removal of Pb(II) from contaminated waters. However, further studies are recommended to be conducted to investigate: (a) influences of other parameters on the removal efficiency of the adsorbent, (b) efficiency of the adsorbent in the removal of other heavy metal ions, and (c) feasibility of using the adsorbent at an industrial scale.

Funding The authors declare that no funds, grants, or other support was received during the preparation of this manuscript.

Data availability The datasets generated during and/or analyzed during the current study are available from the corresponding author on reasonable request.

Declarations

Conflict of interest The authors declare that they have no conflict of interest.

Ethical approval All authors certify that they have ethical conduct required by the journal.

Human and animal rights Not applicable.

Informed consent Not applicable.

References

Abu-Hamdeh NH, Golmohammadzadeh A, Karimipour A (2021) Performing regression-based methods on viscosity of nano-enhanced PCM-Using ANN and RSM. J Market Res 10:1184–1194

Ahmadi S, Mesbah M, Igwegbe CA, Ezeliora CD, Osagie C, Khan NA, Dotto GL, Salari M, Dehghani MH (2021) Sono electro-chemical synthesis of $LaFeO_3$ nanoparticles for the removal of fluoride: optimization and modeling using RSM, ANN and GA tools. J Environ Chem Eng 9(4):105320

Alcalde-Garcia F, Prasher S, Kaliaguine S, Tavares JR, Dumont M-J (2023) Desorption strategies and reusability of biopolymeric adsorbents and semisynthetic derivatives in hydrogel and hydrogel composites used in adsorption processes. ACS Eng Au 3(6):443–460

Alekseeva O, Noskov A, Grishina E, Ramenskaya L, Kudryakova N, Ivanov V, Agafonov A (2019) Structural and thermal properties of montmorillonite/ionic liquid composites. Materials 12(16):2578

Al-Jadir T, Alardhi SM, Al-Sheikh F, Jaber AA, Kadhim WA, Rahim MHA (2023) Modeling of lead (II) ion adsorption on multiwall carbon nanotubes using artificial neural network and Monte Carlo technique. Chem Eng Commun 210(10):1642–1658

Basak M, Rahman ML, Ahmed MF, Biswas B, Sharmin N (2022) The use of X-ray diffraction peak profile analysis to determine the structural parameters of cobalt ferrite nanoparticles using Debye–Scherrer, Williamson–Hall, Halder–Wagner and Size-strain plot: different precipitating agent approach. J Alloys Compd 895:162694

Chang P-H, Mukhopadhyay R, Sarkar B, Mei Y-C, Hsu C-H, Tzou Y-M (2023) Insight and mechanisms of tetracycline adsorption on sodium alginate/montmorillonite composite beads. Appl Clay Sci 245:107127

Cheblaoui R, Mohellebi F, Mameri N (2023) Acetaminophen removal using activated bentonite characterized by (BET, XRF, SEM) and bipolar electrocoagulation: a comparative study application of coupling process on a pharmaceutical effluent. Chem Data Collect 44:100998

Chu Y, Khan MA, Xia M, Lei W, Wang F, Zhu S, Yan X (2020) Synthesis and micro-mechanistic studies of histidine modified montmorillonite for lead (II) and copper (II) adsorption from wastewater. Chem Eng Res Des 157:142–152

Elgarhy AH, Mahran BNA, Liu G, Salem TA, ElSayed EE, Ibrahim LA (2022) Comparative study for removal of phosphorus from aqueous solution by natural and activated bentonite. Sci Rep 12(1):19433

Fan C, Li K, Li J, Ying D, Wang Y, Jia J (2017) Comparative and competitive adsorption of Pb(II) and Cu(II) using tetraethylenepentamine modified chitosan/$CoFe_2O_4$ particles. J Hazard Mater 326:211–220

Fan M, Wang W, Fan X, Peng W, Cao Y, Huang Y, Fan G (2023) Self-assembly regulation of montmorillonite nanosheet for Pb(II) removal from aqueous solution. Powder Technol 430:119000

Foroughi M, Azqhandi MHA (2020) A biological-based adsorbent for a non-biodegradable pollutant: modeling and optimization of Pb (II) remediation using GO-CS-Fe3O4-EDTA nanocomposite. J Mol Liq 318:114077

Foroutan R, Mohammadi R, MousaKhanloo F, Sahebi S, Ramavandi B, Kumar PS, Vardhan KH (2020) Performance of montmorillonite/graphene oxide/$CoFe_2O_4$ as a magnetic and recyclable nanocomposite for cleaning methyl violet dye-laden wastewater. Adv Powder Technol 31(9):3993–4004

Gupta SS, Bhattacharyya KG (2008) Immobilization of Pb (II), Cd (II) and Ni (II) ions on kaolinite and montmorillonite surfaces from aqueous medium. J Environ Manage 87(1):46–58

Hamidi F, Baghani AN, Kasraee M, Salari M, Mehdinejad MH (2023) Modeling, optimization and efficient use of MMT K10 nanoclay for Pb (II) removal using RSM, ANN and GA. Sci Rep 13(1):8434

Huang S-M, Kuo C-H, Chen C-A, Liu Y-C, Shieh C-J (2017) RSM and ANN modeling-based optimization approach for the development of ultrasound-assisted liposome encapsulation of piceid. Ultrason Sonochem 36:112–122

Idehara JYDA, Fagundes DA, Leonel LV, Fernandez-Outon LE, de Mendonça R, Albuquerque AS, Ardisson JD (2023) Investigation of the adsorption of the tetracycline antibiotic by $NiFe_2O_4$ and $CoFe_2O_4$ nanoparticles. Environ Nanotechnol Monitor Manag 20:100830

Irawan C, Nata IF, Lee C-K (2019) Removal of Pb (II) and As (V) using magnetic nanoparticles coated montmorillonite via one-pot solvothermal reaction as adsorbent. J Environ Chem Eng 7(2):103000

Jiang L, Ye Q, Chen J, Chen Z, Gu Y (2018) Preparation of magnetically recoverable bentonite–Fe_3O_4–MnO_2 composite particles for Cd (II) removal from aqueous solutions. J Colloid Interface Sci 513:748–759

Jiang Z-Y, Ma Y-K, Ke Q-F, Chu L-F, Guo C-X, Guo Y-P (2021) Hydrothermal deposition of $CoFe_2O_4$ nanoparticles on activated carbon fibers promotes atrazine removal via physical adsorption and photo-Fenton degradation. J Environ Chem Eng 9(5):105940

Khodosova N, Novikova L, Tomina E, Belchinskaya L, Zhabin A, Kurkin N, Krupskaya V, Zakusina O, Koroleva T, Tyupina E (2022) Magnetic nanosorbents based on bentonite and $CoFe_2O_4$ spinel. Minerals 12(11):1474

Kiraz A, Canpolat O, Erkan EF, Özer Ç (2019) Artificial neural networks modeling for the prediction of Pb (II) adsorption. Int J Environ Sci Technol 16:5079–5086

Kochar C, Taneja L, Yadav PK, Tripathy SS (2023) RSM-CCD approach for optimization study on effective remediation of lead and cadmium from water using surface-modified water caltrop peel biochar. Biomass Conversion Biorefinery. pp 1–19

Larraza I, Lopez-Gonzalez M, Corrales T, Marcelo G (2012) Hybrid materials: magnetite–polyethylenimine–montmorillonite, as magnetic adsorbents for Cr (VI) water treatment. J Colloid Interface Sci 385(1):24–33

Lingamdinne LP, Amelirad O, Koduru JR, Karri RR, Chang Y-Y, Dehghani MH, Mubarak NM (2023a) Functionalized bentonite for removal of Pb (II) and As (V) from surface water: predicting capability and mechanism using artificial neural network. J Water Process Eng 51:103386

Lingamdinne LP, Amelirad O, Koduru JR, Karri RR, Chang Y-Y, Dehghani MH, Mubarak NM (2023b) Functionalized bentonite for removal of Pb(II) and As(V) from surface water: predicting capability and mechanism using artificial neural network. J Water Process Eng 51:103386

Lu L, Xie Y, Yang Z, Chen B (2023) Sustainable decontamination of heavy metal in wastewater and soil with novel rectangular wave asymmetrical alternative current electrochemistry. J Hazard Mater 442:130021

Majiya H, Clegg F, Sammon C (2023) Bentonite-Chitosan composites or beads for lead (Pb) adsorption: design, preparation, and characterisation. Appl Clay Sci 246:107180

Maleki ST, Beigi P, Babamoradi M (2023) Synthesis of pectin hydrogel/Fe_3O_4/Bentonite and its use for the adsorption of Pb (II), Cu (II), and Cd (II) heavy metals from aqueous solutions. Mater Sci Eng, B 298:116899

Manzoor Q, Farrukh MA, Sajid A (2024) Optimization of lead (II) and chromium (VI) adsorption using graphene oxide/ZnO/chitosan nanocomposite by response surface methodology. Appl Surf Sci 655:159544

Moja T, Bunekar N, Mishra S, Tsai T-Y, Hwang S, Mishra A (2020) Melt processing of polypropylene-grafted-maleic anhydride/Chitosan polymer blend functionalized with montmorillonite for the removal of lead ions from aqueous solutions. Sci Rep 10(1):217

Moustafa MT (2023) Preparation and characterization of low-cost adsorbents for the efficient removal of malachite green using response surface modeling and reusability studies. Sci Rep 13(1):4493

Onu CE, Nwabanne JT, Ohale PE, Asadu CO (2021) Comparative analysis of RSM, ANN and ANFIS and the mechanistic modeling in eriochrome black-T dye adsorption using modified clay. S Afr J Chem Eng 36:24–42

Oskui FN, Aghdasinia H, Sorkhabi MG (2019) Modeling and optimization of chromium adsorption onto clay using response surface methodology, artificial neural network, and equilibrium isotherm models. Environ Prog Sustain Energy 38(6):e13260

Prabhu SV, Varadharajan V, Mohanasundaram S, Manivannan S, Khaled JM, Goel M, Srihari K (2023) A comparative study on process optimization of betalain pigment extraction from Beta vulgaris subsp. vulgaris: RSM, ANN, and hybrid RSM-GA methods. Biomass Conversion Biorefinery, pp 1–19

Qin L, Yan L, Chen J, Liu T, Yu H, Du B (2016) Enhanced removal of Pb^{2+}, Cu^{2+}, and Cd^{2+} by amino-functionalized magnetite/kaolin clay. Ind Eng Chem Res 55(27):7344–7354

Raji Z, Karim A, Karam A, Khalloufi S (2023) Adsorption of heavy metals: mechanisms, kinetics, and applications of various adsorbents in wastewater remediation—a review. Waste 1:775–805. https://doi.org/10.3390/waste1030046

Rasoulzadeh H, Dehghani MH, Mohammadi AS, Karri RR, Nabizadeh R, Nazmara S, Kim K-H, Sahu J (2020a) Parametric modelling of Pb (II) adsorption onto chitosan-coated Fe_3O_4 particles through RSM and DE hybrid evolutionary optimization framework. J Mol Liq 297:111893

Rasoulzadeh H, Dehghani MH, Mohammadi AS, Karri RR, Nabizadeh R, Nazmara S, Kim K-H, Sahu JN (2020b) Parametric modelling of Pb(II) adsorption onto chitosan-coated Fe_3O_4 particles through RSM and DE hybrid evolutionary optimization framework. J Mol Liq 297:111893

Ren H, Li H, Fan H, Qi G, Liu Y (2023a) Facile synthesis of $CoFe_2O_4$-graphene oxide nanocomposite by high-gravity reactor for removal of Pb (II). Sep Purif Technol 305:122472

Ren H, Li H, Fan H, Qi G, Liu Y (2023b) Facile synthesis of $CoFe_2O_4$-graphene oxide nanocomposite by high-gravity reactor for removal of Pb(II). Sep Purif Technol 305:122472

Romero-González J, Peralta-Videa JR, Rodríguez E, Delgado M, Gardea-Torresdey JL (2006) Potential of Agave lechuguilla biomass for Cr(III) removal from aqueous solutions: thermodynamic studies. Biores Technol 97(1):178–182

Saber WI, El-Naggar NE-A, El-Hersh MS, El-Khateeb AY, Elsayed A, Eldadamony NM, Ghoniem AA (2021) Rotatable central composite design versus artificial neural network for modeling biosorption of Cr^{6+} by the immobilized Pseudomonas alcaliphila NEWG-2. Sci Rep 11(1):1717

Simsek S, Uslu S, Simsek H (2022) Proportional impact prediction model of animal waste fat-derived biodiesel by ANN and RSM technique for diesel engine. Energy 239:122389

Sultana N, Hossain SZ, Mohammed ME, Irfan M, Haq B, Faruque M, Razzak S, Hossain M (2020) Experimental study and parameters optimization of microalgae based heavy metals removal process using a hybrid response surface methodology-crow search algorithm. Sci Rep 10(1):15068

Tayyebi A, Outokesh M, Moradi S, Doram A (2015) Synthesis and characterization of ultrasound assisted "graphene oxide–magnetite" hybrid, and investigation of its adsorption properties for Sr (II) and Co (II) ions. Appl Surf Sci 353:350–362

Thamer BM, Aldalbahi A, Moydeen M, Al-Enizi AM, El-Hamshary H, El-Newehy MH (2019) Fabrication of functionalized electrospun carbon nanofibers for enhancing lead-ion adsorption from aqueous solutions. Sci Rep 9(1):19467

Tian L, Fu K-B, Chen S, Yao J, Bian L (2022) Comparison of microscopic adsorption characteristics of Zn (II), Pb (II), and Cu (II) on kaolinite. Sci Rep 12(1):15936

Vázquez-Sánchez AY, Lima EC, Abatal M, Tariq R, Santiago AA, Alfonso I, Aguilar C, Vazquez-Olmos AR (2023) Biosorption of Pb (II) using natural and treated Ardisia compressa K. leaves: simulation framework extended through the application of artificial neural network and genetic algorithm. Molecules 28(17):6387

Velarde L, Nabavi MS, Escalera E, Antti M-L, Akhtar F (2023) Adsorption of heavy metals on natural zeolites: a review. Chemosphere 328:138508

Wang A, Chu Y, Muhmood T, Xia M, Xu Y, Yang L, Lei W, Wang F (2018) Adsorption properties of Pb^{2+} by amino group's functionalized montmorillonite from aqueous solutions. J Chem Eng Data 63(8):2940–2949

Wang W, Liu X, Wang X, Zong L, Kang Y, Wang A (2021) Fast and highly efficient adsorption removal of toxic Pb (II) by a reusable porous semi-IPN hydrogel based on alginate and poly (vinyl alcohol). Front Chem 9:662482

Wei W, Wang Q, Li A, Yang J, Ma F, Pi S, Wu D (2016) Biosorption of Pb (II) from aqueous solution by extracellular polymeric substances extracted from Klebsiella sp. J1: adsorption behavior and mechanism assessment. Sci Rep 6(1):31575

Weyrich JN, Mason JR, Bazilevskaya EA, Yang H (2023) Understanding the mechanism for adsorption of Pb (II) ions by Cu-BTC metal–organic frameworks. Molecules 28(14):5443

Yuan P, Fan M, Yang D, He H, Liu D, Yuan A, Zhu J, Chen T (2009) Montmorillonite-supported magnetite nanoparticles for the removal of hexavalent chromium [Cr (VI)] from aqueous solutions. J Hazard Mater 166(2–3):821–829

Zaferani SPG, Emami MRS, Amiri MK, Binaeian E (2019) Optimization of the removal Pb (II) and its Gibbs free energy by thiosemicarbazide modified chitosan using RSM and ANN modeling. Int J Biol Macromol 139:307–319

Zhao X, Zhao H, Huang X, Wang L, Liu F, Hu X, Li J, Zhang G, Ji PJE, Safety E (2021) Effect and mechanisms of synthesis conditions on the cadmium adsorption capacity of modified fly ash. Ecotoxicol Environ Saf 223:112550

Zou C, Jiang W, Liang J, Sun X, Guan Y (2019) Removal of Pb (II) from aqueous solutions by adsorption on magnetic bentonite. Environ Sci Pollut Res 26:1315–1322